Macroscopic Pigmented Skin Lesion Segmentation and Its Influence on Lesion Classification and Diagnosis

Pablo G. Cavalcanti and Jacob Scharcanski

Abstract Melanoma is a type of malignant pigmented skin lesion, and currently is among the most dangerous existing cancers. However, differentiating malignant and benign cases is a hard task even for experienced specialists, and a computer-aided diagnosis system can be an useful tool. Usually, the system starts by pre-processing the image, i.e. removing undesired artifacts such as hair, freckles or shading effects. Next, the system performs a segmentation step to identify the lesion boundaries. Finally, based on the image area identified as lesion, several features are computed and a classification is provided. In this chapter we describe all these steps, giving special attention to segmentation approaches for pigmented skin lesions, proposed for standard camera images (i.e. simple color photographs). Next, we compare the segmentation results to identify which techniques have more accurate results, and discuss how these results may influence in the following steps: the feature extraction and the final lesion classification.

1 Introduction

Pigmented skin lesions include both, benign and malignant forms. According to World Health Organization [1], about 132000 melanoma cases, a dangerous kind of malignant pigmented skin lesion, occur globally each year. The early diagnosis of melanomas is very important for the patient prognosis, since most malignant skin lesion cases can be treated successfully in their early stages. However, research work has shown that discriminating benign from malignant skin lesions is a challenging task [2, 3].

To help diagnosing pigmented skin lesions, physicians often use dermoscopy, which is a non-invasive technique that magnifies submacroscopic structures with

P.G. Cavalcanti (✉) · J. Scharcanski
Instituto de Informática, UFRGS, Av. Bento Gonçalves 9500, Porto Alegre, Brazil
e-mail: pgcavalcanti@inf.ufrgs.br

J. Scharcanski
e-mail: jacobs@inf.ufrgs.br

M.E. Celebi, G. Schaefer (eds.), *Color Medical Image Analysis*,
Lecture Notes in Computational Vision and Biomechanics 6,
DOI 10.1007/978-94-007-5389-1_2,

the help of an optical lens (a dermoscope) and liquid immersion. According to Mayer [4], the use of dermoscopy can increase the diagnosis sensitivity in 10–27 % with respect to the clinical diagnosis. Also, several automatic segmentation and classification methods have been proposed to help obtain a diagnosis with a dermoscopy image [5–10]. However, even with the help of dermoscopy, differentiating malignant and benign lesions is a challenging task. In fact, specialists affirm that in the early evolution stages of malignant lesions, dermoscopy may not be helpful since it often does not improve the diagnosis accuracy [11].

Still considering early stage cases, there are practical situations where a non-specialist (e.g. a physician not trained on Dermatology) wishes to have a qualified opinion about a suspect skin lesion, but only standard camera imaging is available on site. In such situations, telemedicine is justifiable, and the non-specialist can capture a macroscopic pigmented skin lesion (MPSL) image of the suspect skin lesion and send it to a specialist, who can analyze it in higher detail. In this particular situation, a teledermatology consultation brings benefits, like the easier access to health care and faster clinical results [12]. Besides, comparing the physical (face-to-face) patient diagnosis with the remote diagnosis by teledermatology, recent results suggest that teledermatology also tends to be effective and reliable [13].

In the last decades, several segmentation techniques have been proposed to facilitate the remote diagnosis of MPSL images. Since there is no standardized protocol for acquiring these images, often they contain artifacts like hair, shading and other disturbances that make the remote diagnosis by specialists more difficult. With the help of the automatic segmentation, this task may be facilitated. Moreover, the segmentation is an initial step for computer-aided diagnosis systems. Starting from the lesion area identification, lesion features can be extracted and an automatic classification/diagnosis can be provided.

However, since these MPSL images may present characteristics that could make the remote diagnosis more difficult, the automatic processing and analysis also poses some challenges for the researchers in this field. Most of the MPSL image segmentation techniques proposed in the literature convert the original color image to a monochromatic image, and use a thresholding algorithm to identify the lesion area [14–17]. Even more complex segmentation approaches, such as active contours techniques [18, 19], process grayscale images. Nevertheless, the discriminating lesion and healthy skin areas may be more difficult on a monochromatic images, since the chromatic aspect is lacking in them.

In the following sections we will present segmentation algorithms that process multichannel MPSL images, based on thresholding [20] and on level-sets [21]. After that, we show that such methods working on multichannel MPSL images are more efficient than methods working on monochromatic images. Also, we will discuss how features that are relevant from the medical point of view can be extracted, and how the final classification/diagnosis of the acquired lesion is affected by the segmentation quality.

2 Pre-processing

MPSL images usually contain artifacts that make the segmentation process more difficult. Skin characteristics, such as freckles, are easily detected by these algorithms based on color or size. However, most methods available try to identify the lesion area assuming that pigmented skin lesions correspond to locally darker skin discolorations. Consequently, artifacts such as hair and shading, that usually also are darker than healthy skin may be mistaken as lesions during the segmentation process.

Although some of the approaches available eliminate hair as a pre-processing step [15, 16, 19], this task can be performed as a post-processing step, after the image segmentation. Hair is thin, and its shape is quite distinct from the lesion shapes, and consequently it is easy to eliminated hair from MPSL images by morphological operations or other methodologies.

On the other hand, the presence of shading requires pre-processing in advance to segmentation. The shading areas assume any shape, and require a treatment that is different from that given to artifacts like hair. Moreover, if the shading attenuation is well performed, it also contributes for the enhance the contrast between healthy and unhealthy skin.

2.1 Shading Attenuation

Alcón et al. [17] proposed to correct the uneven illumination by removing the low frequency spatial component of the image. Although this method can be efficient for some images, it requires specific parameters. It is very difficult to obtain a specific value that can be used for any input image, and the authors [17] do not detail how to obtain this value automatically.

Face images also are skin images and can be affected by shading effects. Tan and Triggs [22] and Zhou et al. [23] proposed to use Difference of Gaussians (DoG) filtering to correct the shading artifacts. However, this methodology needs specific parameters (e.g., definition of a window size and the filters standard deviations) which may require adjustments for different types of shading effects in the skin lesion images. Moreover, the authors observed that DoG filtering may generate strong-edges in hair areas [22], which could affect negatively the overall segmentation process.

Therefore, Cavalcanti et al. [21] proposed a shading attenuation method that is adaptive to the MPSL image data. Their method assumes that images are acquired in a way that the lesion appears in the image center, and it does not touch the image outer borders. The first step of the method is to convert the image from the original RGB color space to the HSV color space, and retain the Value channel V. This is justified by the fact that this channel presents the higher visibility of the shading effects. A region of 20×20 pixels is extracted from each V corner, and the union of these four sets define the pixel set S. This pixel set is used to adjust the following quadric function $z(x, y)$:

$$z(x, y) = P_1 x^2 + P_2 y^2 + P_3 xy + P_4 x + P_5 y + P_6, \tag{1}$$

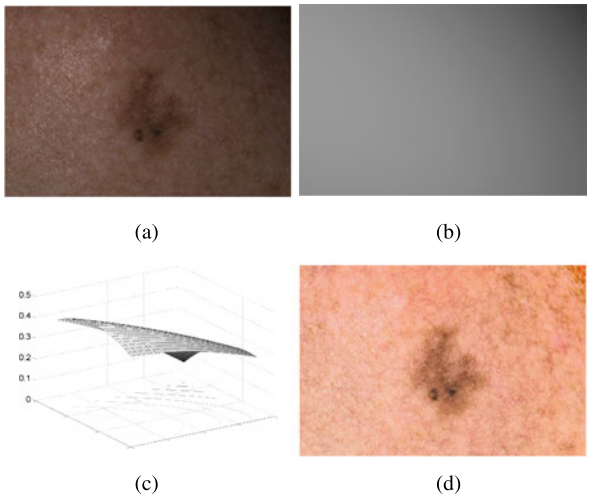

(a) (b) (c) (d)

Fig. 1 Shading attenuation example. (**a**) Input image; (**b**) Obtained quadric model using the corners of the input Value channel; (**c**) Obtained quadric model in 3D; (**d**) Result obtained by the division of the Value channel by the obtained quadric model

where the six quadric function parameters P_i $(i = 1, \ldots, 6)$ are chosen to minimize the error ε:

$$\varepsilon = \sum_{j=1}^{N_s} \left[V(S_{j,x}, S_{j,y}) - z(S_{j,x}, S_{j,y}) \right]^2, \tag{2}$$

where, $S_{j,x}$ and $S_{j,y}$ are the x and y coordinates of the jth element of the set S, respectively, and N_s is the total number of pixels of the four corners (in our case, $N_s = 1600$).

Calculating the quadric function $z(x, y)$ for each image spatial location (x, y), we have an estimate $z(x, y)$ of the local illumination intensity in the image $V(x, y)$. Dividing the original $V(x, y)$ channel by $z(x, y)$, we obtain a new Value channel where the shading effects have been attenuated. The final step is to replace the original Value channel by this new Value channel, and convert the image from the HSV color space to the original RGB color space. In Fig. 1, an example of applying this method to a skin lesion image is presented. The result is a color image easier to be segmented.

3 Segmentation

As already mentioned in Sect. 1, several segmentation techniques have been proposed for MPSL images in the last decades. We outline some representative recent methods and their characteristics in the following subsections. Also, at the end of this section, we present and discuss the performance of these segmentation techniques for a MPSL image database.

3.1 Grayscale-Based Methods

Based on the principle that a pigmented skin lesion is a depigmentation of the skin, and to reduce the computation cost, many segmentation methods start by converting the input image from color to grayscale. After that, most algorithms try to distinguish between healthy to unhealthy pixels. The following techniques illustrate the algorithms that have recently been used for this purpose.

3.1.1 Thresholding-Based Methods

Otsu's Thresholding method [24] has been widely used in grayscale images [14–16]. Furthermore, Cavalcanti et al. [25] also employed this thresholding scheme to the Red channel (R of the RGB color space), trying to take advantage of the fact that healthy skin usually has a reddish tone. This method assumes two pixel classes, namely healthy and unhealthy skin pixels, and searches exhaustively for the threshold th that minimizes the total intra-class variance $\sigma_w^2(th)$, defined as the weighted sum of variances of the two classes:

$$\sigma_w^2(th) = \omega_1(th)\sigma_1^2(th) + \omega_2(th)\sigma_2^2(th), \tag{3}$$

where ω_i are the a priori probabilities of the two classes separated by the threshold th, and σ_i^2 are their intra-class variances. Minimizing the intra-class variance is equivalent to maximizing the inter-class variance $\sigma_b^2(th)$:

$$\begin{aligned}\sigma_b^2(th) &= \sigma^2 - \sigma_w^2(th) \\ &= \omega_1(th)\omega_2(th)\big[\mu_1(th) - \mu_2(th)\big]^2,\end{aligned} \tag{4}$$

where σ^2 is the image pixels variance, and μ_i are the class means. Computed the th threshold, the lesion pixels correspond to the pixels with values lower than th.

The Otsu's method usually is followed by a post-process step, constituted by successive morphological operations, to eliminate other regions that may be thresholded (besides the lesion). Cavalcanti et al. [25] suggest the following procedures: select the largest threshold area, perform a hole filling operation, and a dilation with a disk with 5 pixels of radius.

However, Alcón et al. [17] recently suggested that Otsu's method may oversegment the lesion area. So, they proposed a new thresholding method specific for MPSL images. They observed that, although the lesion intensities distribution $f_l(x)$ is unknown, the distribution $f_s(x)$ of the skin correspond to a Gaussian-like distribution:

$$f_s(x) = Ae^{\frac{-(x-\mu_s)^2}{2\sigma_s^2}}, \tag{5}$$

where, μ_s is the mean value of healthy skin pixel intensities. Being f_{l+s} the distribution of grayscale intensities of the whole image, μ_s is determined by the corresponding intensity value of the highest peak of f_{l+s}. Since $f_{l+s} = f_l + f_s$, and μ_l

(the mean value of lesion pixels) always is lower than μ_s, this distribution can be approximated as:

$$f_{l+s}(x) = \begin{cases} f_s(x), & x \geq \mu_s, \\ f_l(x) + f_s(x), & x < \mu_s. \end{cases} \tag{6}$$

Therefore, based on this assumption, the skin pixels distribution can be estimated as:

$$\widetilde{f}_s(x) = \begin{cases} f_{l+s}(2\mu_s - x), & x < \mu_s, \\ f_{l+s}(x), & x \geq \mu_s, \end{cases} \tag{7}$$

and, consequently, the lesion pixels distribution as:

$$\widetilde{f}_l(x) = f_{l+s}(x) - \widetilde{f}_s(x). \tag{8}$$

Finally, the means $\widetilde{E}(X_s)$ and $\widetilde{E}(X_l)$ of the distributions $\widetilde{f}_s(x)$ and $\widetilde{f}_l(x)$, respectively, are used for the computation of the threshold T as follows:

$$T = \frac{\widetilde{E}(X_s) + \widetilde{E}(X_l)}{2}, \tag{9}$$

and, as in the Otsu's method, the pixels with values lower than the computed threshold, are segmented as lesion pixels.

Figure 2 illustrates the performance of the above mentioned thresholding-based segmentation methods. As can be observed, these low-complexity algorithms are able to determine the lesion area, suffering from boundary definition inaccuracies caused by hair. Also, it is important to observe that the method proposed by Alcon et al. is negatively affected by the lack of a post-processing method to eliminate undesired thresholded areas. Finally, Fig. 2(i) shows the difference between Otsu and Alcon et al. results, obtained by thresholding different regions of the histogram.

3.1.2 Multi-Direction GVF Snake Method

Some researchers have proposed to use Snakes (or Active-Contours) methods to segmented MPSL images, instead of a thresholding method [19]. These methods usually start by smoothing the image, and as an illustration of such methods we refer to the method proposed by Tang [19]. In this method, the MPSL image is initially smoothed by adaptive anisotropic diffusion filtering. Tang modified the traditional anisotropic diffusion to make it more robust to noise, and more details can be found in [19]. Next, a modification of the traditional GVF (Gradient Vector Flow) snake [26] is used to determine the lesion boundary. The original GVF (u, v) can be determined by the minimization of the following energy function:

$$\begin{aligned} E_{GVF}(u,v) = \frac{1}{2} \int\int & g\big(|\nabla f|\big)\big(u_x^2 + u_y^2 + v_x^2 + v_y^2\big) \\ & + \big(1 - g\big(|\nabla f|\big)\big)\big((u - f_x)^2 + (v - f_y)^2\big) dx dy, \end{aligned} \tag{10}$$

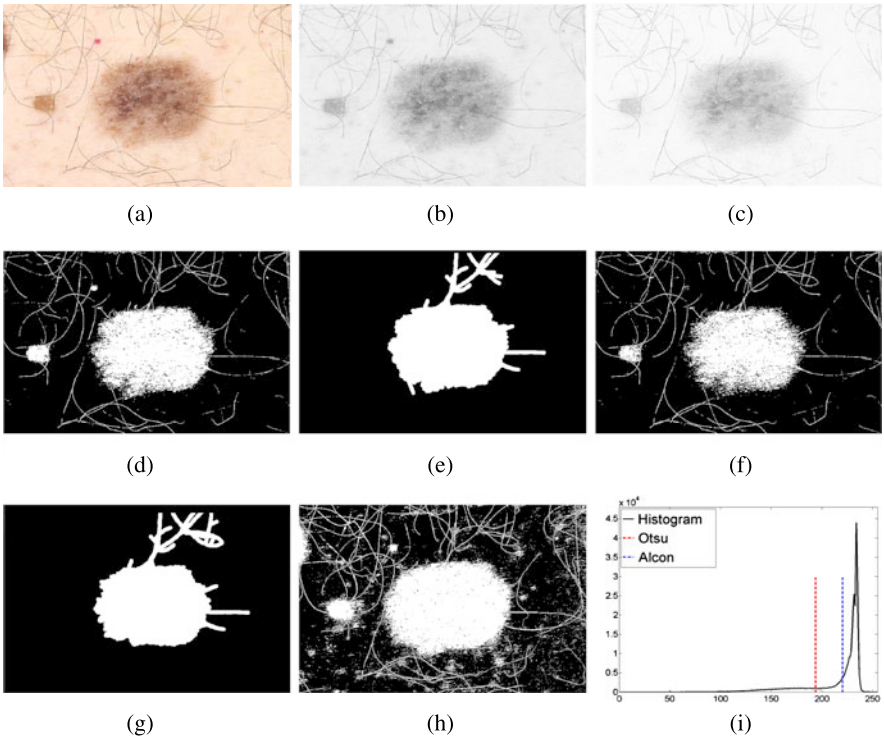

Fig. 2 MPSL image segmentation using thresholding-based methods. (**a**) The RGB image after pre-processing. (**b**) Figure (**a**) after conversion to grayscale. (**c**) The Red channel of (**a**). (**d**) The resultant binary mask of Otsu's method applied to figure (**b**). (**e**) The result of applying morphological operation in (**d**). (**f**) The resultant binary mask of Otsu's method applied to figure (**c**). (**g**) The result of applying morphological operation in (**f**). (**h**) The resultant binary mask of Alcon et al. method applied to figure (**b**). (**i**) The plot of histogram of figure (**b**), and the computed Otsu and Alcon thresholds

where, f is an edge map derived from the image, g is an edge-force magnitude:

$$g\big(|\nabla f|\big) = \exp\left(-\left(\frac{|\nabla f|}{K}\right)\right), \tag{11}$$

and K is a non-negative smoothing parameter for the field (u, v).

Tang uses a Multi-Directional GVF (MDGVF) in order to create a force-field (u, v) that enforces the snake to converge to the lesion area, and not to spurious image edges. Based on an initialization mask (containing a rough segmentation of the lesion), the author computes the lesion center $(\overline{x}, \overline{y})$ and the direction vector $\mathbf{d}(x, y) = (d_x, d_y)$ at each image pixel (x, y), pointing to the lesion center:

$$d_x = \frac{\overline{x} - x}{\sqrt{(\overline{x} - x)^2 + (\overline{y} - y)^2}}, \tag{12}$$

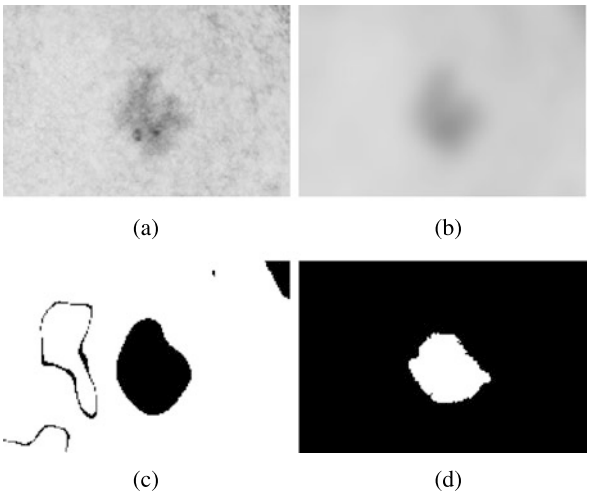

Fig. 3 MPSL image segmentation using multi-direction GVF snake method. (**a**) An example of image after pre-processing and grayscale conversion. (**b**) Image (**a**) after the application of anisotropic diffusion filter. (**c**) The rough segmentation of (**b**). (**d**) The final segmentation after the snake convergence

$$d_y = \frac{\overline{y} - y}{\sqrt{(\overline{x} - x)^2 + (\overline{y} - y)^2}}. \tag{13}$$

After that, the author determines the unitary vector $\mathbf{v}(x, y) = (v_x, v_y)$ for each pixel closer to $\mathbf{d}(x, y)$ by cosine similarity, i.e. $\mathbf{v}(x, y)$ is one of the nine vectors $(-1, -1)$, $(-1, 0)$, $(-1, 1)$, $(0, -1)$, $(0, 0)$, $(0, 1)$, $(1, -1)$, $(1, 0)$ or $(1, 1)$.

Being $I(x, y)$ the grayscale intensity of a pixel (x, y), its respective directional gradient DI can be determined as follows:

$$DI(x, y) = I(x + v_x, y + v_y) - I(x, y). \tag{14}$$

Since often lesions are darker than healthy skin, the negative values of this gradient can be used to determine a new edge-map:

$$F(x, y) = \begin{cases} DI(x, y), & \text{if } DI(x, y) < 0, \\ 0, & \text{otherwise.} \end{cases} \tag{15}$$

Replacing f by F in Eq. (10), a new energy function is obtained to force the snake to converge specifically along the direction of the lesion. To initialize this process, Tang suggests using the Multistage Adaptive Thresholding method [27] to segment the image roughly. In Fig. 3, we present a typical lesion segmentation obtained using this method. The reader may observe that this algorithm handles better artifacts like hair than thresholding-based methods, but unfortunately the lesion boundary is not well determined.

3.2 Multichannel-Based Methods

Although grayscale images have widely being used for segmenting MPSL images, some approaches rely on multichannel images as described in the following sections.

3.2.1 Thresholding-Based Methods

In a similar way that thresholding is used in grayscale MPSL images, we can threshold color images. In this case, thresholds are computed and a binary mask is generated for each channel, and masks are combined to form the final color MPSL image segmentation. However, working with color images adds new concerns. For example, pigmented skin lesions are not easily discriminated from healthy skin on the Green channel (G of the RGB color space), and the color information may disturb instead of benefiting the final results.

So, to facilitate the use of thresholding methods, Cavalcanti and Scharcanski [20] recently proposed a multichannel image representation for MPSL images that maximizes the discrimination between healthy and unhealthy skin regions. The idea is to create a new 3-channel image $\bar{I}_i^N$ based on the normalization of the RGB channels $\bar{I}_i^C$ of the input image, and then use a thresholding algorithm based on Otsu's method to segment it.

The first channel is a representation of the image darkness, relying on the fact that lesion areas are depigmented skin regions. Each pixel is defined as $\bar{I}_1^N(x, y) = 1 - \bar{I}_i^C(x, y)$, i.e. the complement of the normalized Red channel.

The second channel is a texture representation, since local textural variability usually is higher in lesions than in healthy skin areas. Being $\bar{L}$ a normalized Luminance image defined by the average of the three $\bar{I}_i^C$ channels, the textural variability in $\bar{L}(x, y)$ can be quantified by computing $\tau(x, y, \sigma)$ as follows:

$$\tau(x, y, \sigma) = \bar{L}(x, y)\frac{\widetilde{S}(x, y, \sigma)}{S(x, y, \sigma)}, \tag{16}$$

where, $S(x, y, \sigma) = \bar{L}(x, y) * G(\sigma)$ (i.e., the Luminance image $\bar{L}$ is smoothed by a Gaussian filter with standard deviation σ), and $\widetilde{S}(x, y, \sigma)$ represents its complement. In this way, if an image region is dark, its textural information is emphasized; if the region is bright, its textural information is de-empshasized. However, a single Gaussian filter may not be sufficient to capture the textural variability, so $\tau(x, y, \sigma)$ is calculated for different σ values and we select its maximum value at each pixel:

$$T(x, y) = \max_{\sigma}\big[\tau(x, y, \sigma)\big], \quad \sigma \in \{\sigma_1, \sigma_2, \ldots, \sigma_N\}. \tag{17}$$

Finally, the texture variation channel T is normalized, obtaining $\bar{I}_2^N(x, y)$ as follows:

$$\bar{I}_2^N(x, y) = \big(T(x, y) - \min(T)\big)/\big(\max(T) - \min(T)\big). \tag{18}$$

The third channel $\bar{I}_3^N(x, y)$ of the representation describes the local color variation, assuming that healthy and unhealthy skin regions present different color distributions. The Principal Component Analysis (PCA) method is applied on the normalized colors of the image $\bar{I}_i^C(x, y)$, and the first component is retained (i.e. the component that maximizes the local data variance). In this representation, lesion pixels usually have higher variability values than healthy skin pixels, and to detect

these lesion pixels in this channel (corresponding to those detected in channels $\bar{I}_1^N$ and $\bar{I}_2^N$), the following PCA property described next is utilized. Since the input data is centered around the mean, and healthy skin pixels often are more frequent in the MPSL image, the projections of the healthy skin pixels on the PCA space tend to generate values nearer to zero than the lesion pixels (i.e., the projected lesion pixels tend to have larger magnitudes, i.e. positive or negative). Therefore, the color variability information C is represented by the pixel projection magnitudes, and the normalization of C generates the $\bar{I}_3^N$ channel:

$$\bar{I}_3^N(x,y) = \big(C(x,y) - \min(C)\big)/\big(\max(C) - \min(C)\big). \tag{19}$$

Also, the $\bar{I}_3^N$ channel is filtered with a 5×5 median filter to reduce the noise. Obtained this multichannel representation, the Otsu's thresholding method (see Sect. 3.1.1) is used to segment the image. Three thresholds th_i are computed, one for each channel $\bar{I}_i^N(x,y)$, and a pixel (x,y) is defined as part of a lesion region (i.e., $\phi(x,y) = 1$) if its value is higher than the threshold th_i in at least two of the three channels:

$$\phi(x,y) = \begin{cases} 1, & \text{if } (\bar{I}_1^N(x,y) > th_1 \wedge \bar{I}_2^N(x,y) > th_2), \\ 1, & \text{if } (\bar{I}_2^N(x,y) > th_2 \wedge \bar{I}_3^N(x,y) > th_3), \\ 1, & \text{if } (\bar{I}_1^N(x,y) > th_1 \wedge \bar{I}_3^N(x,y) > th_3), \\ 0, & \text{otherwise.} \end{cases} \tag{20}$$

As mentioned before (see Sect. 2), after thresholding the remaining skin artifacts (such as freckles and hair) are eliminated more easily. These artifacts usually occur in isolated regions that differ in area and perimeter from skin lesions, since lesions often have larger areas and more irregular boundaries. Therefore, the perimeter and the area of all thresholded connected pixel sets (i.e. where $\phi(x,y) = 1$) are computed, and then this set of regions is partitioned in two clusters. All regions in the cluster with smaller areas (in average) are eliminated, and their correspondent mask pixels are set to $\phi(x,y) = 0$. At the end, the resultant mask is filtered by a 5×5 median filter, eliminating any possible remaining artifacts that may originate rim imperfections.

In Fig. 4, we present the results for all steps of this method, including the multichannel representation generation, the thresholding and post-processing steps. The reader may observe that the lesion boundary is determined with higher precision in comparison to the methods presented previously.

3.2.2 ICA-Based Active-Contours Method

Instead of creating a multichannel representation for a MPSL color image, Cavalcanti et al. [21] recently proposed a segmentation method to be used on the image original color channels. They proposed to use a classical active-contours method (Chan-Vese [28]), followed by morphological operations as a post-processing step.

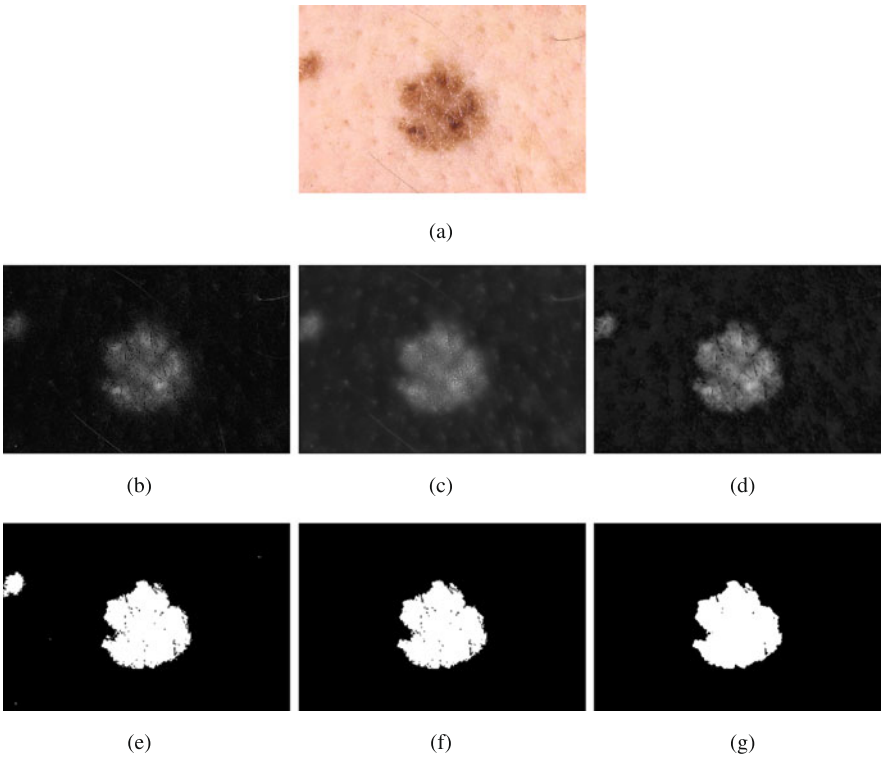

Fig. 4 Segmentation process for the image shown in (**a**) using thresholding method on a multichannel representation. In (**b**)–(**d**), respectively, the $\bar{I}_i^N$ channels representing darkness, texture variation and color variation. In (**e**)–(**g**), respectively, binary masks after thresholding, artifacts elimination and filtering

Active-contours methods have already been used to segment pigmented skin lesion images. However, as we seen in Sect. 3.1.2, usually a conversion to a grayscale image precedes the processing stages. Other approaches have been proposed using color images [29], but these algorithms were designed for dermoscopic images, which have different characteristics, and a common drawback of such methods is the difficulty to determine a convenient way to initialize the active-contours algorithm. If the initialization do not indicate the lesion regions with some accuracy, the final segmentation may be incorrect and include healthy skin regions.

Cavalcanti et al. [21] proposed to use independent component analysis (ICA) to generate a reliable binary mask for initializing the active-contours algorithm. They observed that when ICA is applied to a MPSL image, one of the resultant ICA components corresponds mainly to the lesion area, the second component to the healthy skin, and the third component corresponds to noise artifacts. Nevertheless, there is an ordering indeterminacy inherent to the ICA method, and it is not possible to know in advance which component will show the lesion more clearly. However, due

to the lesion variability, the histogram of the component that shows more clearly the lesion often has a non-Gaussian histogram (frequently multimodal). The noise artifacts component histogram tends to be non-Gaussian, and the component that shows healthy skin more clearly tends to have a Gaussian histogram. Thus, they estimate the non-Gaussianity of the ICA histogram components with differential entropy, i.e. $\mathcal{J}(X) = |H(X) - H(X_g)|$, where X_g is a Gaussian distributed random variable with the same variance as X. The component that produces the largest differential entropy (i.e., contains the highest non-Gaussianity estimate) is identified as the one containing the lesion information more clearly, and the smallest differential entropy component carries basically healthy skin.

After reordering the channels, the lesion region is best represented in the first channel. Next, the component values are normalized in the range [0, 1], and the Otsu's thresholding method is used (see Sect. 3.1.1) to segment the skin lesion in this channel. Given the ICA results, the lesion information can be emphasized (closer to value 1) or de-emphasized (closer to value 0) in this channel, and consequently the thresholded area may correspond to either, the lesion or the background. To guarantee that the lesion is captured in the thresholded area, the corner pixels (used in the shading attenuation step, that are known to correspond to healthy skin) are tested to check if they are thresholded as '1's or '0's. If most corner pixels are thresholded as '1's, the thresholded area corresponds to healthy skin, and the logical complement is used to obtain the lesion localization mask. In this way, a rough approximation of the lesion area is obtained. Next, the lesion boundary is better approximated and possible artifacts are eliminated with a morphological opening (i.e. the structuring element is a disk with a radius of 3 pixels).

Given this initialization binary mask, Cavalcanti et al. [21] proposed determining the lesion boundary more precisely using the Chan-Vese Active-contours method for vector-valued images [28]. Their method assumes that the color image I_i is formed by two regions of approximately constant intensities c_1 and c_2, separated by a curve C. The lesion localization mask is used as an initialization, indicating approximately the region to be segmented. Afterwards, the active-contours method iteratively tries to minimize the energy function $F(c_1, c_2, C)$ in the color image I_i:

$$F(c_1, c_2, C) = \mu\, length(C) + \lambda_1 \int_{inside(C)} \frac{1}{3} \sum_{i=1}^{3} \left| I_i(x, y) - c_{1,i} \right|^2 dxdy$$

$$+ \lambda_2 \int_{outside(C)} \frac{1}{3} \sum_{i=1}^{3} \left| I_i(x, y) - c_{2,i} \right|^2 dxdy,$$

where μ, λ_1 and λ_2 are weighting parameters ($\lambda_1 = \lambda_2 = 1$, as suggested in [28], and $\mu = 0.2$). Using the Level-set formulation, it is possible to minimize the energy function embedding the curve C, obtaining the zero level set $C(t) = \{(x, y) | \phi(t, x, y) = 0\}$ of a higher dimensional Level-set function $\phi(t, x, y)$. The evolution of $\phi(t, x, y)$ is given by the following motion Partial Differential Equation:

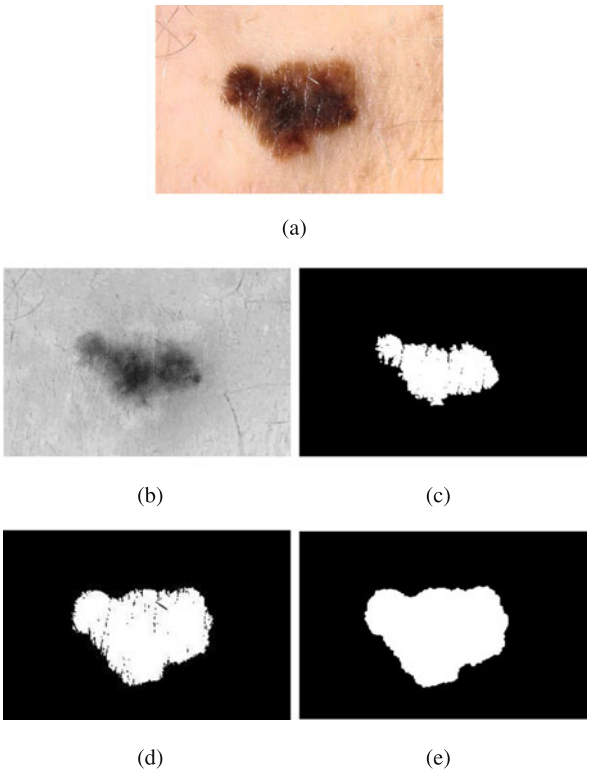

Fig. 5 Illustration of the segmentation using the ICA-Based Active-Contours method. (**a**) Color image after shading attenuation. (**b**) First re-ordered independent component/channel of image (**a**). (**c**) Lesion localization mask. (**d**) The active-contours segmentation result. (**e**) Final lesion segmentation, after post-processing image (**d**)

$$\frac{\partial \phi}{\partial t} = \delta_\varepsilon(\phi)\left[\mu \,\mathrm{div}\left(\frac{\nabla \phi}{|\nabla \phi|}\right) - \frac{1}{3}\sum_{i=1}^{3}\lambda_1 \left|I_i(x,y) - c_{1,i}\right|^2 + \frac{1}{3}\sum_{i=1}^{3}\lambda_2 \left|I_i(x,y) - c_{2,i}\right|^2\right], \tag{21}$$

where $\delta_\varepsilon(\phi)$ is the Dirac delta function, $c_{1,i}$ and $c_{2,i}$ are the averages inside and outside of the curve C in the i-th channel I_i, respectively.

It is possible that the final curve C contains regions beyond the lesion area. So, if the number of regions segmented by the Chan-Vese method is higher than one, local artifacts are eliminated. The area and the perimeter of each segmented region are computed, and these values are clustered with K-Means, where $K = 2$. The regions in the cluster with the smaller areas (in average) are eliminated as artifacts and the other regions are kept. The regions kept are hole filled to improve their connectivity, forming the final segmentation mask. The final post-processing step is a morphological dilation (with a disk of 5 pixels of radius as the structuring element).

In Fig. 5, we present the results for all steps of this method. The reader may observe that the initialization mask already do not contain skin artifacts, forcing the active-contours method to a precise determination of the lesion area.

3.3 Comparison of Segmentation Methods Based on Experimental Results

In order to compare the performances of the six state-of-art segmentation methods for MPSL images presented above, we use the same image dataset as in Alcón et al. [17], which contains 152 images that have been collected from the Dermnet dataset [30]. This dataset consists of 107 melanomas and 45 Clark nevi (or atypical nevi), a benign kind of lesion that present similar characteristics to melanomas.

We implemented the shading attenuation step and all the presented algorithms, and processed all the 152 images with these implemented methods. Some examples of segmentation results can be seen in Fig. 6. We also measured the error for each resultant segmentation using the following criterion [6–8]:

$$\varepsilon = \frac{Area(Segmentation \oplus GroundTruth)}{Area(GroundTruth)} \times 100\ \%, \tag{22}$$

where, *Segmentation* is the result of the method in test, *GroundTruth* is the manual segmentation of the same lesion, $Area(S)$ denotes the number of pixels indicated as lesion in the segmentation result S, and $\oplus$ indicates the exclusive-OR, operation that gives the pixels for which the *Segmentation* and *GroundTruth* disagree.

The average error obtained by each segmentation method is presented in Table 1. We also included a synopsis of the six segmentation methods tested in Table 1. As can be seen, the only method that uses color information (ICA-Based Active-Contours Method) generates the smallest error segmentation, in average. Although the methods based on the Otsu's Thresholding Method are not computationally as intense as the method based on active-contours, those methods appear in the sequence, as those with the smallest segmentation errors (multichannel representation appears to be more effective than the methods based on grayscale images). The thresholding method proposed by Alcón et al. and the Multi-Direction GVF Snake method were ranked last, since these methods presented higher segmentation errors. It shall be observed that these methods do not have a post-processing step. Analyzing the segmentation results visually (see Fig. 6), we may observe that the lack of a segmentation post-processing step to eliminate artifacts usually generate segmentations larger than the lesion itself.

Besides the average errors, we present in Table 2 the percentage of images in the database that had lesion segmentation errors lower than 5 %, 10 %, 20 %, 30 % and 40 %, respectively. As can be seen, the Otsu's thresholding method applied on grayscale images tends to be more accurate, but potentially it also can generate larger segmentation errors than the ICA-Based Active-Contours method (the only method that uses color MPSL images). On the other hand, the ICA-Based Active-Contours method tends to be more reliable in the sense that it is less likely to produce large segmentation errors, and obtained experimentally the most accurate lesion segmentation results (in average).

Considering the results presented in Tables 1 and 2, we can infer that color can contribute to improve the segmentation of a MPSL image. Although methods based on one single channel may segment accurately some MPSL images, in average the

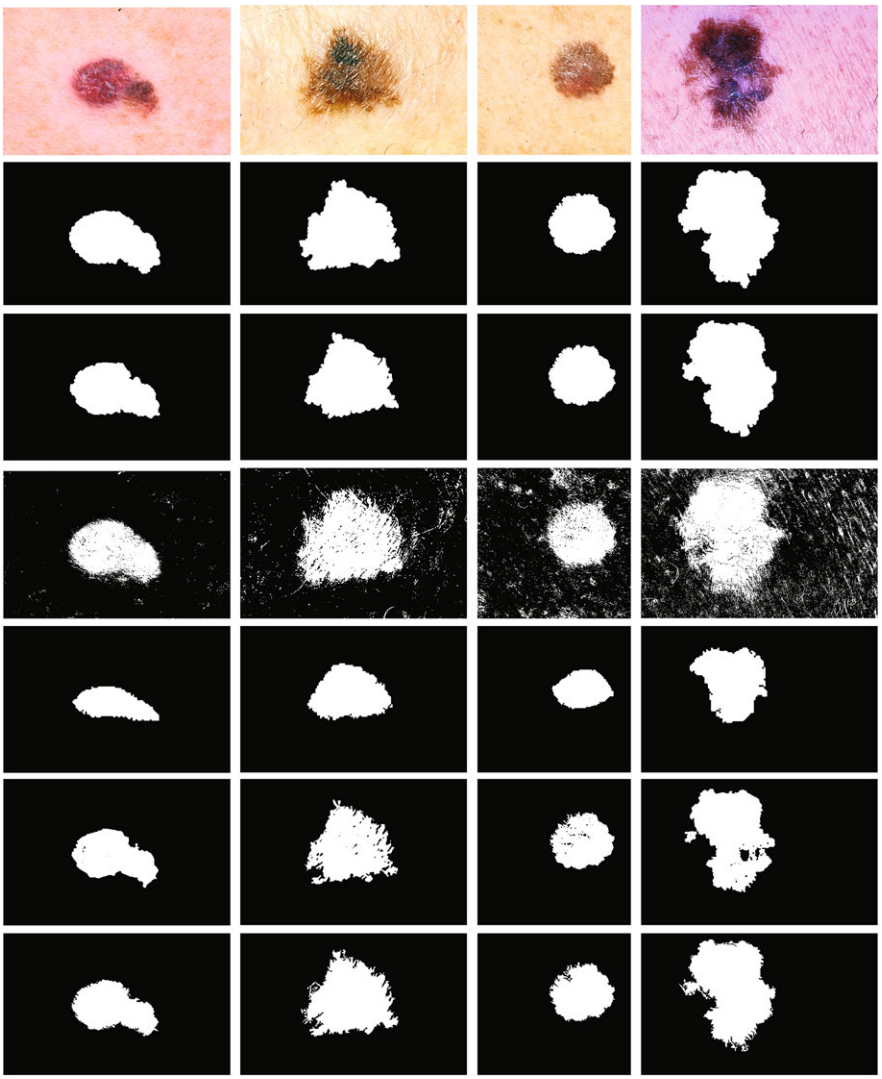

Fig. 6 Examples of MPSL images and their respective segmentation results for the six presented methods. In the *1st. line*, the color images (after shading attenuation). *From 2nd. to 7th. lines*, respectively, results of Otsu's Thresholding Method on Grayscale, Otsu's Thresholding Method on the Red Channel, Alcón et al. Thresholding Method, Multi-Direction GVF Snake Method, Thresholding Method on a Multichannel Representation, and ICA-Based Active-contours Method

color-based method provides more reliable segmentation results. In the next sections, we discuss if the segmentation accuracy is correlated, or not, to the final classification/diagnosis accuracy.

Table 1 Comparison of the six segmentation methods tested for the MPSL image database

Approach	Image type	Post-processing type	Computational cost	ε in average
Otsu's Thresholding Method on Grayscale [15]	Monochromatic	M. Morphology	Low	42.33 %
Otsu's Thresholding Method on the Red Channel [25]	Monochromatic	M. Morphology	Low	38.58 %
Alcón et al. Thresholding Method [17]	Monochromatic	–	Low	165.31 %
Multi-Direction GVF Snake Method [19]	Monochromatic	–	High	59.60 %
Thresholding Method on a Multichannel Representation [20]	Multichannel	M. Morphology	Medium	34.83 %
ICA-Based Active-Contours Method [21]	Multichannel (Color)	M. Morphology	High	28.34 %

Table 2 Segmentation errors in terms of error percentages

Approach	$\varepsilon < 5$ %	$\varepsilon < 10$ %	$\varepsilon < 20$ %	$\varepsilon < 30$ %	$\varepsilon < 40$ %
ICA-Based Active-Contours Method [21]	3.29 %	29.61 %	73.68 %	86.84 %	94.08 %
Otsu's Thresholding Method on Grayscale [15]	3.29 %	34.87 %	75.66 %	87.50 %	93.42 %
Otsu's Thresholding Method on the Red Channel [25]	1.97 %	27.63 %	67.11 %	83.55 %	93.42 %
Thresholding Method on a Multichannel Representation [20]	1.32 %	4.61 %	43.42 %	69.74 %	81.58 %
Alcón et al. Thresholding Method [17]	0.00 %	0.00 %	8.55 %	16.45 %	25.00 %
Multi-Direction GVF Snake Method [19]	0.00 %	0.00 %	0.00 %	5.92 %	23.03 %

4 Feature Extraction for Skin Lesion Discrimination

Given a MPSL image segmentation, we are able to obtain a classification (or diagnosis) of the acquired pigmented skin lesion. Before obtaining this classification, features representative of the skin lesion must be extracted. Computer-aided diagnosis systems often try to reproduce computationally the ABCD rule [31], which is an acronym referring to the four criteria used in clinical diagnosis, namely: **A**symmetry, **B**order Irregularity, **C**olor Variation and **D**ifferential Structures. Several approaches have been proposed for describing quantitatively the first three criteria [3, 5, 8, 17, 32]. These feature extraction techniques can be used jointly to rep-

resent benign and malignant cases better, and discriminate them more effectively. The fourth criterion (i.e. Differential structures) only is visible in dermoscopy images, but to describe quantitatively this lesion characteristic automatically still is challenging.

Since our ultimate goal is to evaluate the influence of image segmentation on the final classification/diagnosis, we will adopt the feature extraction and classification scheme proposed specifically for MPSL images by Cavalcanti and Scharcanski [20]. In the following sections we present the 52 features that have been used in their ABCD rule implementation, also including features that were proposed by other authors. In terms of terminology, it is important to clarify that images $\bar{I}_i^C$ and $\bar{I}_i^N$ refer to a normalized color image and to the multichannel image representation presented in Sect. 3.2.1, respectively.

4.1 Features Used for Lesion Asymmetry Characterization

The goal of these features is to quantify the lesion shape, in special the asymmetry of the lesion in relation to the principal axes. The major axis L_1 of the lesion is aligned with its longest diameter, passing through its center; the minor axis L_2 is orthogonal to L_1 and also passes through the shape center. The features utilized are the following:

f_1: Solidity: the ratio between the lesion area (A) and its convex hull area [17];
f_2: Extent: the ratio between the lesion area and its bounding box area [17];
f_3: Equivalent diameter: $4A/(L_1\pi)$ [5, 17];
f_4: Circularity: $4\pi A/(L_1 p)$, where p is the lesion perimeter [17];
f_5: The ratio between the principal axes (L_2/L_1) [5, 17];
f_6: The ratio between sides of the lesion bounding box [17];
f_7: The ratio between the lesion perimeter p and its area A [3];
f_8: $(B_1 - B_2)/A$, where, B_1 and B_2 are the areas in each side of axis L_1;
f_9: Similar to f_8, but makes use of the shorter axis L_2;
f_{10}: $B1/B2$ with respect to the axis L_1;
f_{11}: Similar to f_{10}, but makes use of the shorter axis L_2.

4.2 Features Used for Lesion Boundary Irregularity Characterization

The boundary sharpness is quantified by the magnitude of the gradient $|\nabla \vec{\bar{I}}_i^N|$ at each pixel using the Sobel operator [20]. However, instead of using pixels only at the lesion rim, we analyze pixels in an extended (dilated) rim[1] [17]. Consequently,

[1]The rim is dilated by 2 pixels, producing a 5 pixels wide region centered at the lesion rim, as suggested in [17].

lesions that have a smooth boundary (usually nevi) are better characterized. Also, the lesion boundary dilation makes the boundary representation more robust to the inaccuracies of the segmentation process. To characterize the lesion boundary irregularity, the following features are used [20]:

f_{12}–f_{14}: Average gradient magnitude of the pixels in the lesion extended rim [17], in each one of the three $\bar{I}_i^N$ channels;
f_{15}–f_{17}: Variance of the gradient magnitude of the pixels in the lesion extended rim [17], in each one of the three $\bar{I}_i^N$ channels;

The lesion rim irregularity is characterized in the ABCD rule by dividing the rim in 8 symmetric regions [31]. In addition to the two principal axes L_1 and L_2, two additional axes are obtained by rotating by 45 degrees these orthogonal axes. Therefore, 8 symmetric regions $R = 1, \ldots, 8$ are generated. For each channel $\bar{I}_i^N$, the average gradient magnitudes of the extended rim pixels $\mu_{R,i}$ $(R = 1, \ldots, 8)$ are computed. Therefore, 6 more features are calculated:

f_{18}–f_{20}: Average of the 8 $\mu_{R,i}$ values in each one of the three $\bar{I}_i^N$ channels;
f_{21}–f_{23}: Variance of the 8 $\mu_{R,i}$ values in each one of the three $\bar{I}_i^N$ channels;

4.3 Features Used for Lesion Color Variation Characterization

These features quantify the color variation in the lesion, and the following measurements can be utilized for this purpose [20]:

f_{24}–f_{27}: Maximum, minimum, mean and variance of the pixels intensities inside the lesion segment in the color variation channel $\bar{I}_3^N$;
f_{28}–f_{39}: Maximum, minimum, mean and variance of the pixels intensities inside the lesion segment in each one of three original $\bar{I}_i^C$ channels;
f_{40}–f_{42}: Ratios between mean values of the tree original $\bar{I}_i^C$ channels: $mean(\bar{I}_1^C)/mean(\bar{I}_2^C)$, $mean(\bar{I}_1^C)/mean(\bar{I}_3^C)$ and $mean(\bar{I}_2^C)/mean(\bar{I}_3^C)$, considering only pixels inside the lesion segment.

Physicians usually identify six distinct hues in skin lesions: white, red, light and dark brown, blue-gray, and black [31]. Lesions containing more of these hues are more likely to be malignant. The lesion color variability can be quantified by computing the occurrence of these typical hues within a lesion segment. Given a pixel in the lesion segment, the nearest reference color (associated with a typical hue, see Table 3 [17]) is found by the Euclidean distance to the pixel color in $\bar{I}_i^C$. A hue occurrence counter is created, one cell per typical hue. For each lesion pixel, the nearest typical hue counter is increased by 1. Finally, typical hues counters are normalized/divided by the lesion area A, and generate the 6 additional features f_{43}–f_{48}.

Table 3 Six possible colors of a lesion on the RGB color space

Color	Red	Green	Blue
White	1	1	1
Red	0.8	0.2	0.2
Light Brown	0.6	0.4	0
Dark Brown	0.2	0	0
Blue-Gray	0.2	0.6	0.6
Black	0	0	0

4.4 Features Used for Lesion Differential Structures Characterization

The lesion differential structures refer to submacroscopic morphologic and vascular structures only visible in dermoscope images. In an attempt to extract the characteristics of these structures also on a macroscopic image, differences between benign and malignant lesions can be measured using texture features. Cavalcanti and Scharcanski [20] propose to extract the 4 features $f_{49}-f_{52}$, namely the maximum, minimum, mean and variance of the pixels intensities inside the lesion segment to represent the textural variation in the channel $\bar{I}_2^N$.

4.5 Feature Extraction Summary

Even for specialized physicians the discrimination of benign from malignant pigmented skin lesions may not be an easy task, and the development of techniques that facilitate this job is a current research topic. In the previous sections, we presented 52 features that help in this task, but readers can probably find additional (or even alternative) features in literature, and probably new features will be proposed in the coming years as this research area develops. The ultimate goal is to represent image lesion characteristics to could facilitate the early classification/diagnosis and reduce the number of deaths caused by these lesions.

Another important issue when dealing with the selection of feature sets is the adoption of automatic (or interactive) feature selection algorithms. Some authors of classification approaches for pigmented skins lesions [5, 15, 17] suggest using a method to select the best features as those that help most the MPSL image class discrimination. However, this feature selection procedure can be tricky. Pigmented skin lesions have a large variability in terms of characteristics, and the discrimination between a malignant and a benign case can be determined by only 1 or 2 features. If these features have been eliminated because they did not seem to be important on a given training set, malignant cases can be incorrectly classified as benign, leading to costly false negatives.

5 Classification of Pigmented Skin Lesion Images

After extracting the features that characterize each MPSL image, we can use these data to obtain a final classification (or diagnosis) of the imaged lesion. We discuss how this information is processed in the following sections.

5.1 Feature Normalization

The extracted features may have values in different ranges. Some of the proposed approaches do not perform feature normalization [8, 17]. However, classifiers tend to be more efficient if these feature values are normalized and represented in the same range (i.e., the feature values are scaled to fall in a specified range), therefore we adopt this normalization step in our work.

This feature value scaling is performed based on the mean and standard deviation of the captured feature values [5, 20, 32]. Among the possible feature normalization options [32, 33], we chose to normalize the feature values using the well known z-score transformation [33]:

$$Z_{i,j} = \frac{((v_{i,j} - \mu_j)/(3\sigma_j) + 1)}{2}, \tag{23}$$

where, $v_{i,j}$ is the value of the jth feature of the ith sample (image), μ_j and σ_j are the mean and standard deviation of the jth feature, respectively. After the z-score transformation, most of the $Z_{i,j}$ values are in the $[0, 1]$ range. The out-of-range values are saturated to either 0 or 1.

5.2 Defining Training Sets

Classification techniques are commonly used in machine learning. The validation test requires the definition of training sets, and two methodologies are usually applied, namely: cross-validation and holdout validation [34]. The cross-validation method divides the samples in S portions, and $S - 1$ portions are used for training while the remaining portion is used for testing. This process is repeated until all the samples have been evaluated. In the holdout validation, part of the samples in each class (benign or malignant) are randomly selected and used for training, and the remaining samples are used for testing. Often, up to half of the initial sample set is used for testing. The holdout validation method was used in our experiments described in Sect. 6.

However, a common limitation of the public domain MPSL datasets is the relatively small number of cases, specially in the benign class (which often leads to unbalanced training sets). So, in addition to the selection of representative samples, we often need to balance and extend the training sets. One popular alternative is to add

new training samples using the Smoothed Bootstrap Resampling method [20, 35]. This method is used when there are not enough samples to guarantee the statistical significance of the data set. In this case, the original samples are randomly selected, and new ones are created by adding a small amount of zero-centered noise to their feature values, enlarging the data set [35]. In our experiments (see Sect. 6), we used zero mean Gaussian noise, with $\sigma = 0.1$, and made sure to obtain at least 2500 samples for each class (5000 samples in total) for a two class problem.

5.3 Classification Methods

After the feature normalization and the training samples selection steps, the generated data is the input used to train a classification method. For the classification of pigmented skin lesions images (macroscopic or dermoscopic), Support Vector Machines (SVM) is frequently utilized [5, 16]. However, due to the complex class shapes generated by the feature data, determining an adequate kernel and its parameters often is a difficult task. Artificial Neural Networks [15, 36] suffer from a similar limitation, determining the number of layers in multilayer perceptrons and their characteristics is critical, and may increase or decrease the final accuracy significantly. However, techniques such Decision and Regression Trees [17] usually are less computationally intensive, and the parameters can be determined automatically. However, despite of their relatively simplicity, such classifier used alone hardly obtain the desirable accuracy levels by state-of-the-art of MPSL classification schemes.

In our experiments, where we try to relate segmentation and classification performance, we used a Nearest Neighbor Classifier (KNN) with $K = 1$. This algorithm is very simple, where each sample/image is assigned to its neighbor class using the Euclidean Distance in feature space. This method was chosen for its simplicity and because it has been already used successfully in pigmented skin lesion image classification research [20, 36, 37].

6 Discussion of Experimental Evidences: Pigmented Skin Lesion Segmentation and Its Influence on the Lesion Classification and Diagnosis

In the previous sections, we discuss the procedures utilized to obtain a classification/diagnosis for a MPSL image, from the pre-processing steps to the final classification. Now, we wish to evaluate the influence of the segmentation methods in the final lesion classification/diagnosis.

Recall that the Alcón et al. dataset used in our experiments (see Sect. 3.3) contains 107 melanoma images (malignant cases) and 45 Clark nevi images (benign cases). In Tables 4, 5, 6 and 7 we present the classification results for these 152

Table 4 Comparison of classification results in average

Approach	Sensitivity	Specificity	Accuracy
Alcón et al. Thresholding Method [17]	92.56 %	89.16 %	91.55 %
Otsu's Thresholding Method on Grayscale [15]	93.89 %	83.91 %	90.93 %
ICA-Based Active-Contours Method [21]	92.95 %	85.60 %	90.78 %
Thresholding Method on a Multichannel Representation [20]	93.91 %	83.29 %	90.76 %
Multi-Direction GVF Snake Method [19]	92.34 %	86.89 %	90.72 %
Otsu's Thresholding Method on the Red Channel [25]	94.17 %	80.36 %	90.08 %

Table 5 Best classification results in terms of sensitivity

Approach	Sensitivity	Specificity	Accuracy
Otsu's Thresholding Method on the Red Channel [25]	99.07 %	75.56 %	92.11 %
Alcón et al. Thresholding Method [17]	99.07 %	75.56 %	92.11 %
Multi-Direction GVF Snake Method [19]	98.13 %	86.67 %	94.74 %
Thresholding Method on a Multichannel Representation [20]	98.13 %	86.67 %	94.74 %
ICA-Based Active-Contours Method [21]	98.13 %	84.44 %	94.08 %
Otsu's Thresholding Method on Grayscale [15]	97.20 %	80.00 %	92.11 %

Table 6 Best classification results in terms of specificity

Approach	Sensitivity	Specificity	Accuracy
Alcón et al. Thresholding Method [17]	92.52 %	97.78 %	94.08 %
ICA-Based Active-Contours Method [21]	92.52 %	95.56 %	93.42 %
Multi-Direction GVF Snake Method [19]	87.85 %	93.33 %	89.47 %
Thresholding Method on a Multichannel Representation [20]	93.46 %	91.11 %	92.76 %
Otsu's Thresholding Method on Grayscale [15]	94.39 %	88.89 %	92.76 %
Otsu's Thresholding Method on the Red Channel [25]	94.39 %	88.89 %	92.76 %

images obtained by different state-of-the-art methods. In each one of these Tables, we present the Sensitivity (i.e, the percentage of MPSL images correctly classified in the malignant class), Specificity (i.e., the percentage of MPSL images correctly classified in the benign class) and Accuracy (i.e., the percentage of MPSL images correctly classified overall, considering all images).

Since the training sample selection process is random (see Sect. 5.2), and may not assure that the selected samples represent well the characteristics of both classes, we considered as representative all the 50 training sets obtained in 50 random trails, as well as the 50 classification results corresponding to each one of these training sets.

Table 7 Best classification results in terms of accuracy

Approach	Sensitivity	Specificity	Accuracy
Alcón et al. Thresholding Method [17]	98.13 %	88.89 %	95.39 %
Thresholding Method on a Multichannel Representation [20]	98.13 %	86.67 %	94.74 %
ICA-Based Active-Contours Method [21]	97.20 %	88.89 %	94.74 %
Multi-Direction GVF Snake Method [19]	97.20 %	88.89 %	94.74 %
Otsu's Thresholding Method on Grayscale [15]	96.26 %	88.89 %	94.08 %
Otsu's Thresholding Method on the Red Channel [25]	94.39 %	88.89 %	92.76 %

That is, we computed 50 times: (a) the training samples selection, (b) the Smoothed Bootstrap Resampling method, and (c) the Nearest Neighbor classifier results, so that our experimental results are statistically relevant. The final classification performance is measured based on these 50 trials.

We present the Accuracy, Specificity and Sensitivity averages of the 50 obtained results in Table 4. In Tables 5, 6 and 7, we present the best classification results for each segmentation method tested (in terms of Sensitivity, Specificity and Accuracy, respectively). As can be seen, these segmentation methods were ranked based on their segmentation (see Sect. 3) and classification errors, but their segmentation and classification rankings differ. This indicates that the MPSL image feature set describes the lesions well, representing well their morphology even if the segmentation is not as precise as would be desirable. Additionally, these experimental results show that better feature extraction techniques that could take advantage of more accurate segmentations are needed, achieving classification results that are more accurate.

It shall be observed that our classification results indicate accuracies higher than 90 % (in average), independent of the selected segmentation algorithm. These accuracies are higher than the diagnosis accuracies obtained by trained physicians in telemedicine, which range between 31 % to 85 % according to the literature [13].

7 Summary and Future Trends

In this chapter, we reviewed the procedures used for classifying or diagnosing a pigmented skin lesion from a macroscopic image. Given the acquired color image, we showed how to eliminate shading effects, determine the lesion boundaries and some of the important lesion characteristics, and how to obtain the correct lesion classification as a (malignant) melanoma or a (benign) nevus.

The importance of using color also is outlined in this work, since the use of color can enhance the MPSL image segmentation precision. It shall be observed that the classification accuracies obtained in such segmentation and classification schemes already can be higher than the diagnosis accuracies obtained by trained physicians in

telemedicine. Although the segmentation results do not correlate well with the final classification accuracies, we believe that in future new features can be developed to make better use of more precise segmentations, leading even higher classification accuracies.

In particular, we believe that such automatic MPSL image analysis schemes will contribute to increase the reliability of telemedicine. Consequently, the access to MPSL image prescreening systems shall be increase in the near future, which will contribute to improve the current early skin cancer detection rates, the skin cancer patient prognosis, and also it shall help increase the efficiency of the medical care systems.

References

1. World Health Organization. How commom is skin cancer? http://www.who.int/uv/faq/skincancer/en/index1.html
2. Rao BK, Marghoob AA, Stolz W, Kopf AW, Slade J, Wasti Q, Schoenbach SP, De-David M, Bart RS (1997) Can early malignant melanoma be differentiated from atypical melanocytic nevi by in vivo techniques? Skin Res Technol 3(1):8–14
3. Fikrle T, Pizinger K (2007) Digital computer analysis of dermatoscopical images of 260 melanocytic skin lesions; perimeter/area ratio for the differentiation between malignant melanomas and melanocytic nevi. J Eur Acad Dermatol Venereol 21:48–55
4. Mayer J (1997) Systematic review of the diagnostic accuracy of dermatoscopy in detecting malignant melanoma. Med J Aust 167:206–210
5. Celebi ME, Kingravi HA, Uddin B, Iyatomi H, Aslandogan YA, Stoecker WV, Moss RH (2007) A methodological approach to the classification of dermoscopy images. Comput Med Imaging Graph 31(6):362–373
6. Celebi ME, Kingravi HA, Iyatomi H, Aslandogan YA, Stoecker WV, Moss RH, Malters JM, Grichnik JM, Marghoob AA, Rabinovitz HS, Menzies SW (2008) Border detection in dermoscopy images using statistical region merging. Skin Res Technol 14:347–353
7. Gomez DD, Butakoff C, Ersboll BK, Stoecker W (2008) Independent histogram pursuit for segmentation of skin lesions. IEEE Trans Biomed Eng 55:157–161
8. Iyatomi H, Oka H, Celebi M, Hashimoto M, Hagiwara M, Tanaka M, Ogawa K (2008) An improved internet-based melanoma screening system with dermatologist-like tumor area extraction algorithm. Comput Med Imaging Graph 32(7):566–579
9. Zhou H, Schaefer G, Sadka A, Celebi M (2009) Anisotropic mean shift based fuzzy c-means segmentation of dermoscopy images. IEEE J Sel Top Signal Process 3:26–34
10. Zhou H, Schaefer G, Celebi ME, Lin F, Liu T (2011) Gradient vector flow with mean shift for skin lesion segmentation. Comput Med Imaging Graph 35(2):121–127
11. Skvara H, Teban L, Fiebiger M, Binder M, Kittler H (2005) Limitations of dermoscopy in the recognition of melanoma. Arch Dermatol 141:155–160
12. Massone C, Wurm EMT, Hofmann-Wellenhof R, Soyer HP (2008) Teledermatology: an update. Semin Cutan Med Surg 27:101–105
13. Whited JD (2006) Teledermatology research review. Int J Dermatol 45:220–229
14. Manousaki AG, Manios AG, Tsompanaki EI, Panayiotides JG, Tsiftsis DD, Kostaki AK, Tosca AD (2006) A simple digital image processing system to aid in melanoma diagnosis in an everyday melanocytic skin lesion unit: a preliminary report. Int J Dermatol 45:402–410
15. Ruiz D, Berenguer VJ, Soriano A, Martin J (2008) A cooperative approach for the diagnosis of the melanoma. In: Proceedings of the 30th annual international conference of the IEEE engineering in medicine and biology society (EMBC), vol 2008, pp 5144–5147

16. Tabatabaie K, Esteki A, Toossi P (2009) Extraction of skin lesion texture features based on independent component analysis. Skin Res Technol 15:433–439
17. Alcon JF, Ciuhu C, ten Kate W, Heinrich A, Uzunbajakava N, Krekels G, Siem D, de Haan G (2009) Automatic imaging system with decision support for inspection of pigmented skin lesions and melanoma diagnosis. IEEE J Sel Top Signal Process 3:14–25
18. Parolin A, Herzer E, Jung C (2010) Semi-automated diagnosis of melanoma through the analysis of dermatological images. In: 23rd conference on graphics, patterns and images (SIBGRAPI), pp 71–78
19. Tang J (2009) A multi-direction gvf snake for the segmentation of skin cancer images. Pattern Recognit 42:1172–1179
20. Cavalcanti PG, Scharcanski J (2011) Automated prescreening of pigmented skin lesions using standard cameras. Comput Med Imaging Graph 35(6):481–491
21. Cavalcanti PG, Scharcanski J, Persia LED, Milone DH (2011) An ica-based method for the segmentation of pigmented skin lesions in macroscopic images. In: Proceedings of the 33rd annual international conference of the IEEE engineering in medicine and biology society (EMBC)
22. Tan X, Triggs B (2010) Enhanced local texture feature sets for face recognition under difficult lighting conditions. IEEE Trans Image Process 19:1635–1650
23. Zhou H, Miller P, Zhang J (2011) Age classification using radon transform and entropy based scaling svm. In: Proceedings of the British machine vision conference. BMVA Press, Guildford, pp 28.1–28.12. doi:10.5244/C.25.28
24. Otsu N (1979) A threshold selection method from gray-level histograms. IEEE Trans Syst Man Cybern 9:62–66
25. Cavalcanti P, Yari Y, Scharcanski J (2010) Pigmented skin lesion segmentation on macroscopic images. In: Proceedings of the 25th international conference on image and vision computing, New Zealand
26. Xu C, Prince JL (1998) Snakes, shapes, and gradient vector flow. IEEE Trans Image Process 7(3):359–369
27. Yan F, Zhang H, Kube CR (2005) A multistage adaptive thresholding method. Pattern Recognit Lett 26:1183–1191
28. Chan TF, Sandberg BY, Vese LA (2000) Active contours without edges for vector-valued images. J Vis Commun Image Represent 11(2):130–141
29. Silveira M, Nascimento J, Marques J, Marcal A, Mendonca T, Yamauchi S, Maeda J, Rozeira J (2009) Comparison of segmentation methods for melanoma diagnosis in dermoscopy images. IEEE J Sel Top Signal Process 3:35–45
30. Dermnet skin disease image atlas. http://www.dermnet.com
31. Nachbar F, Stolz W, Merkle T, Cognetta AB, Vogt T, Landthaler M, Bilek P, Braun-Falco O, Plewig G (1994) The abcd rule of dermatoscopy: high prospective value in the diagnosis of doubtful melanocytic skin lesions. J Am Acad Dermatol 30(4):551–559
32. Ganster H, Pinz P, Rohrer R, Wildling E, Binder M, Kittler H (2001) Automated melanoma recognition. IEEE Trans Med Imaging 20:233–239
33. Aksoy S, Haralick RM (2000) Probabilistic vs. geometric similarity measures for image retrieval. In: Proceedings of the IEEE conference on computer vision and pattern recognition, 13–15 June 2002, vol 2, pp 357–362
34. Bishop CM (2007) Pattern recognition and machine learning, 1st edn. Information science and statistics. Springer, Berlin
35. Young GA (1990) Alternative smoothed bootstraps. J R Stat Soc, Ser B, Methodol 52(3):477–484
36. Dreiseitl S, Ohno-Machado L, Kittler H, Vinterbo S, Billhardt H, Binder M (2001) A comparison of machine learning methods for the diagnosis of pigmented skin lesions. J Biomed Inform 34:28–36
37. Burroni M, Corona R, Dell'Eva G, Sera F, Bono R, Puddu P, Perotti R, Nobile F, Andreassi L, Rubegni P (2004) Melanoma computer-aided diagnosis: reliability and feasibility study. Clin Cancer Res 10:1881–1886

http://www.springer.com/978-94-007-5388-4

Color Medical Image Analysis
Celebi, M.E.; Schaefer, G. (Eds.)
2013, X, 206 p., Hardcover
ISBN: 978-94-007-5388-4